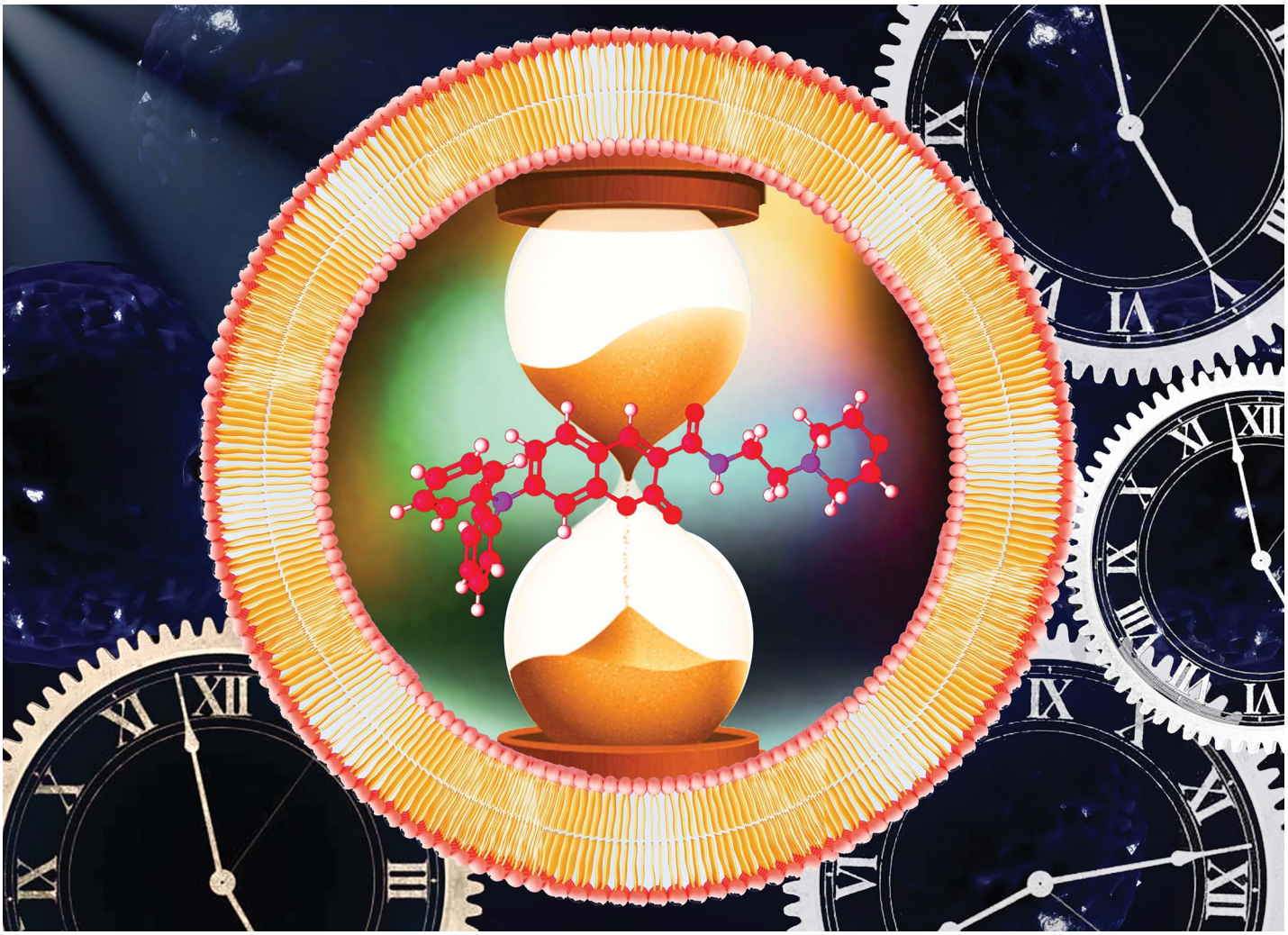

Showcasing research from Professor Abhijit Patra's laboratory, Department of Chemistry, Indian Institute of Science Education and Research Bhopal (IISERB), Madhya Pradesh, India.

Unveiling autophagy and aging through time-resolved imaging of lysosomal polarity with a delayed fluorescent emitter

A lysosome-specific coumarin-diphenylamine-based thermally activated delayed fluorescent probe, DC-Lyso, exhibiting a polarity-sensitive fluorescence lifetime has been developed. It was employed for the specific long-term tracking of lysosomal dynamics, including lysosome-mitochondrion and lysosome-lipid droplet interactions under physiological conditions. The microsecond timescale imaging using the delayed fluorescence of DC-Lyso nanoparticles in water further reveals the distribution of lysosomal polarity in various cancerous cell lines and a model organism, *Caenorhabditis elegans*. The lysosomal polarity has been elucidated as an indicator of the complex aging process in a multicellular organism, *C. elegans*.

As featured in:

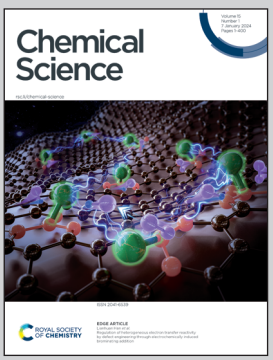

See Abhijit Patra *et al.*, *Chem. Sci.*, 2024, **15**, 102.

ROYAL SOCIETY OF CHEMISTRY

rsc.li/chemical-science

Registered charity number: 207890

Chemical Science

ROYAL SOCIETY OF CHEMISTRY

EDGE ARTICLE

View Article Online
View Journal | View Issue

Cite this: *Chem. Sci.*, 2024, **15**, 102

All publication charges for this article have been paid for by the Royal Society of Chemistry

Unveiling autophagy and aging through time-resolved imaging of lysosomal polarity with a delayed fluorescent emitter†

Subhadeep Das, Abhilasha Batra, Subhankar Kundu, Rati Sharma and Abhijit Patra *

Detecting the lysosomal microenvironmental changes like viscosity, pH, and polarity during their dynamic interorganelle interactions remains an intriguing area that facilitates the elucidation of cellular homeostasis. The subtle variation of physiological conditions can be assessed by deciphering the lysosomal microenvironments during lysosome–organelle interactions, closely related to autophagic pathways leading to various cellular disorders. Herein, we shed light on the dynamic lysosomal polarity in live cells and a multicellular model organism, *Caenorhabditis elegans* (*C. elegans*), through time-resolved imaging employing a thermally activated delayed fluorescent probe, DC-Lyso. The highly photostable and cytocompatible DC-Lyso rapidly labels the lysosomes (within 1 min of incubation) and exhibits red luminescence and polarity-sensitive long lifetime under the cellular environment. The distinct variation in the fluorescence lifetime of DC-Lyso suggests an increase in local polarity during the lysosomal dynamics and interorganelle interactions, including lipophagy and mitophagy. The lifetime imaging analysis reveals increasing lysosomal polarity as an indicator for probing the successive development of *C. elegans* during aging. The *in vivo* microsecond timescale imaging of various cancerous cell lines and *C. elegans*, as presented here, therefore, expands the scope of delayed fluorescent emitters for unveiling complex biological processes.

Received 15th May 2023
Accepted 11th November 2023

DOI: 10.1039/d3sc02450d

rsc.li/chemical-science

Introduction

Lysosomes are one of the most acidic organelles of cells, containing various hydrolase enzymes that play pivotal roles in the degradation of damaged proteins, organelles, and macromolecules during autophagy.[1,2] Lysosomal functioning requires an optimum balance of their microenvironments like viscosity, pH, and polarity of the medium.[2–5] Under physiological conditions, these highly dynamic lysosomes maintain organelle interactions among themselves as well as with lipid droplets and mitochondria, to regulate cellular homeostasis, which may result in significant lysosomal microenvironmental changes.[5–12] Moreover, abnormal lysosomal functionality can cause unusual micropolarity changes, leading to the initiation of lysosomal storage disorders, cardiovascular diseases, neurodegeneration, and various types of cancers.[13–17] Thus, the quantitative visualization of lysosomal microenvironment variation is crucial for the early-stage detection of any cellular disorder.[5,14–18] The unique spatial distribution of sub-cellular microenvironments during autophagic pathways can be assessed quantitatively using time-resolved fluorescence imaging (TRFI).[19–23] In this context, molecular probes with long lifetimes are promising for fluorescence lifetime imaging microscopy (FLIM), effectively eliminating the short-lived signals arising from the cellular environment and providing a better signal-to-noise ratio.[10,24–28]

Triplet harvesting materials,[29–33] specially, all-organic thermally activated delayed fluorescence (TADF) emitters, are emerging candidates for various optoelectronic[34–39] and biomedical applications, including micro-to-millisecond TRFI.[25–28] TADF probes with donor–acceptor (D–A) or donor–π–acceptor (D–π–A) linkages with twisted molecular structures enable intramolecular charge transfer (ICT).[34–37] The localized frontier molecular orbitals in such systems lower the energy of the excited singlet (S_1) state leading to a decrease in the singlet–triplet energy gap (ΔE_{ST}).[34–38] The low ΔE_{ST} facilitates the triplet (T_1) harvesting *via* S_1 to T_1 intersystem crossing (ISC), followed by the thermally controlled reverse intersystem crossing (RISC, $T_1 \rightarrow S_1$) and subsequently resulting in delayed fluorescence.[40–42] Nevertheless, the O_2-mediated quenching of the triplet state, hydrophobicity, and longer incubation time of the TADF emitters restrict their use for monitoring real-time

Department of Chemistry, Indian Institute of Science Education and Research (IISER) Bhopal, Bhopal, Madhya Pradesh, 462066, India. E-mail: abhijit@iiserb.ac.in

† Electronic supplementary information (ESI) available: Synthesis, characterizations, and spectroscopic data, including transient absorption, time-resolved emission, temperature, and laser power-dependent studies of DC-Lyso, MTT assay, JC-1 assay, intracellular imaging, lysosomal dynamics, FLIM imaging of lipophagy and mitophagy, and *C. elegans* and delayed fluorescence imaging at microsecond time domain; Movies S1 and S2. See DOI: https://doi.org/10.1039/d3sc02450d

organelle dynamics under diverse physiological conditions.[10,25–28] Moreover, the nonspecific staining and lack of environment-sensitive emission properties under biological conditions remain a substantial challenge in tracking organelle dynamics and associated micropolarity changes using TADF emitters.[10,26,43]

Linking organelle targeting units to the TADF-core without affecting the D–A electronic communication could be an effective strategy to target subcellular organelles.[27,44] Herein, a morpholine-functionalized coumarin-diphenylamine-based TADF-probe, DC-Lyso, was synthesized for the specific imaging of lysosomes. DC-Lyso displayed polarity-dependent transient decay properties along with low cytotoxicity and rapid cellular internalization (1 min incubation). The large Stokes shift, red emission under cellular environment, long lifetime, photostability, and cytocompatibility of the probe make it suitable for background-free tracking of lysosomal dynamics. The FLIM images revealed the fluorescence lifetime variations during lysosomal dynamics, including lipophagy and mitophagy, signifying the real-time lysosomal polarity changes. Moreover, lysosomal polarity variations were probed as an indicator of a complex biological process, aging, in soil nematodes *Caenorhabditis elegans* (*C. elegans*). Employing the stable delayed fluorescence properties at ambient aqueous conditions, the distribution of lysosomal polarity was also shown at the microsecond time domain in different cancerous cell lines (HeLa, A549, and CHO) and *C. elegans* using DC-Lyso nanoparticles. The current study, thus, introduces a new strategy to employ a lysosome-specific TADF probe for deciphering the subtle cellular microenvironments during interorganelle interactions and aging.

Results and discussion

Considering our target of probing lysosomal polarity under diverse physiological conditions, DC-Lyso was designed and synthesized by fine-tuning the donor–acceptor (D–A) architecture, resulting in solvent-specific intramolecular charge transfer (Scheme 1). The coumarin backbone was chosen due to its electron-deficient nature and availability of different substitution sites, whereas the diphenylamine (DPA) unit was considered for its electron-rich nature and donor ability. We anticipated that the donor (DPA) substitution at the C-7 position of the acceptor coumarin ring might result in a twisted geometry around the D–A linkage and electronically decoupled frontier molecular orbitals (Fig. S1†). Moreover, the weakly basic morpholine unit ($pK_a = 5–6$) covalently linked to the D–A unit could be attributed to the specific lysosome targeting ability of the probe without altering the electronic communication between the donor and the acceptor.[10] DC-Lyso was synthesized starting from 4-bromo salicylaldehyde and diethyl malonate in a four-step process involving Claisen-condensation, hydrolysis, amidation, and subsequently Buchwald–Hartwig coupling between the resultant precursor and diphenylamine (Schemes S1–S4, Fig. S54–S65†).

The optimized molecular structure of DC-Lyso demonstrated a dihedral angle of ~35° between the donor and acceptor units

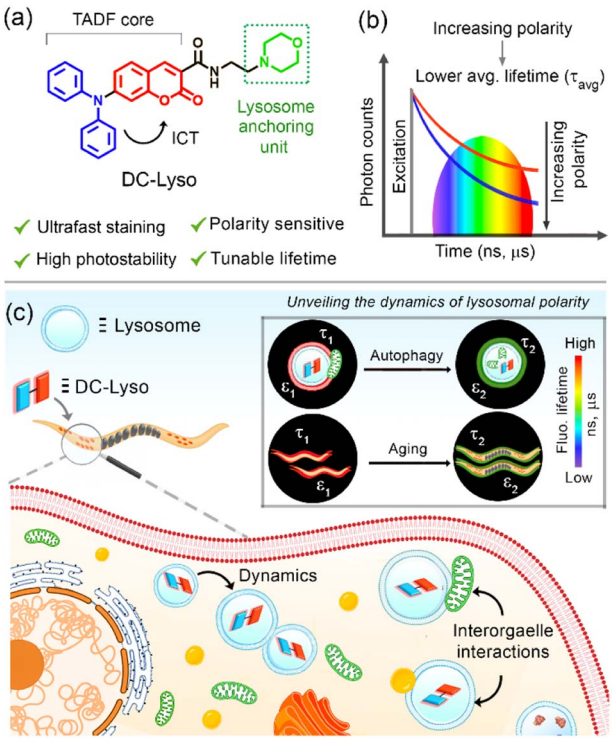

Scheme 1 (a) Salient features of lysosome-targeting thermally activated delayed fluorescent (TADF) probe, DC-Lyso. The intramolecular charge transfer (ICT) from the donor (D, diphenylamine, blue) to the acceptor (A, coumarin, red) results in a low singlet–triplet energy gap (ΔE_{ST}) and polarity sensitive fluorescence lifetime (τ_{avg}). (b) Illustration depicting the relative variation of average fluorescence lifetime of DC-Lyso as a function of solvent polarity. (c) Pictorial depiction of the new findings of the current study towards the elucidation of dynamic lysosomal polarity as an indicator of complex biological processes like autophagy and aging through the polarity-sensitive lifetime of DC-Lyso using fluorescence lifetime imaging microscopy.

(Fig. S1b†). The HOMO (−5.33 eV) was predominantly localized on the donor DPA with a relatively small distribution over the benzene ring of the coumarin moiety (Fig. S1c†). However, the LUMO (−1.98 eV) was solely located on the acceptor coumarin unit (Fig. S1c†). The small overlap of the HOMO and LUMO suggests the possibility of ICT characteristics. The time-dependent density functional theory (TDDFT) calculations revealed a low ΔE_{ST} value of 0.21 eV, indicating the possibility of facile ISC and RISC pathways (Fig. S2a†).

DC-Lyso showed two distinct absorption bands located at ~300 nm (7.4×10^4 M^{-1} cm^{-1}) and ~400 nm (9.6×10^4 M^{-1} cm^{-1}, Fig. 1a, S4 and Table S1†). The absorption band located at ~300 nm was ascribed to the π–π* transitions of the donor and acceptor cores (Fig. S4a†), whereas the broad, featureless, red-shifted band at ~400 nm suggested an ICT absorption due to the charge separation in the ground state (Fig. 1a and S4b†).[45,46] DC-Lyso showed a featureless emission band with a large Stokes shift, typically associated with excited-state charge transfer (Fig. 1a). Moreover, the emission maxima gradually red shifted as the polarity of the medium increased from hexane ($\lambda_{em} = 458$ nm) to dimethyl sulfoxide (DMSO, λ_{em}

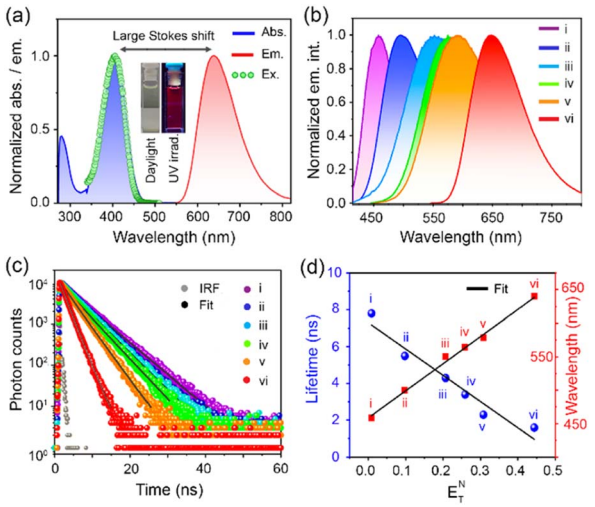

Fig. 1 (a) Normalized absorption (blue), emission (red, $\lambda_{ex} = 408$ nm), and excitation spectra (green, $\lambda_{ex} = 640$ nm) of DC-Lyso in dimethyl sulfoxide (DMSO); inset: digital photograph of DC-Lyso in DMSO under daylight and UV-irradiation at 365 nm. (b) Normalized emission spectra, and (c) photoluminescence (PL) decay of DC-Lyso at nanosecond timescale in organic solvents of varying polarity. (d) Reichardt's plot depicting the linear dependence of fluorescence lifetime and emission wavelength of DC-Lyso with normalized solvent polarity parameter, E_T^N. For (b–d): (i) hexane, (ii) toluene, (iii) tetrahydrofuran, (iv) chloroform, (v) dichloromethane, and (vi) DMSO; concentration: 2 μM.

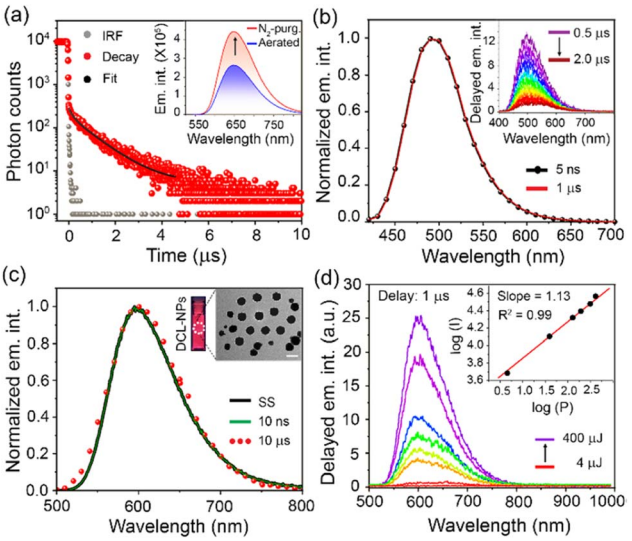

Fig. 2 (a) Microsecond timescale photoluminescence (PL) decay of DC-Lyso in deoxygenated DMSO; inset: enhancement of emission intensity in prolonged N_2 purged deoxygenated DMSO solution (red, $\lambda_{ex} = 408$ nm, $T = 298$ K) in comparison to the aerated solution (blue). (b) Time-resolved emission spectra (TRES) of DC-Lyso ($\lambda_{ex} = 408$ nm) in deoxygenated toluene sliced at 5 ns (black) and 1 μs (red) ascertaining the microsecond timescale emission as delayed fluorescence; inset: TRES analysis of DC-Lyso at different timescales (0.5 → 2 μs) in deoxygenated toluene recorded with an intensified charge-coupled device (iCCD) camera. (c) Normalized steady-state emission (SS, black line, $\lambda_{ex} = 470$ nm, $T = 298$ K), TRES recorded at 10 ns (green line) and 10 μs (red dots) time delays of the aqueous dispersion of DCL-NPs, ascertaining the delayed fluorescence; inset: a digital photograph of DCL-NPs in water under UV-irradiation at 365 nm, and transmission electron microscopy (TEM) image of DCL-NPs, scale = 100 nm. (d) Laser fluence-dependent delayed emission spectra (time delay = 1 μs) of the aqueous dispersion of DCL-NPs; inset: linear fitting of the delayed emission intensity of DCL-NPs as a function of laser power suggesting the unimolecular dependency of the emission intensity ($\lambda_{ex} = 470$ nm, $T = 298$ K). For (a–d), the concentration of DC-Lyso = 2 μM.

= 640 nm, Fig. 1b). The large bathochromic shifts, increasing full width of half maxima ($FWHM_{Hexane} = 67$ nm to $FWHM_{DMSO} = 127$ nm), and decreasing quantum yield in polar solvents suggested the stabilization of the excited ICT state leading to the facile nonradiative deactivations (Fig. 1b, S6 and Table S2†).[47–53] In accordance with these observations, the average fluorescence lifetime of DC-Lyso decreased gradually at the nanosecond timescale with increasing solvent polarity due to the enhanced nonradiative (k_{nr}) relaxations in polar solvents (Fig. 1c and Table S3†).[54,55] Interestingly, the average fluorescence lifetime showed a linear relation with the Reichardt's normalized solvent polarity parameter (E_T^N, Fig. 1c, d and S6†).[47,54] The linear dependence of fluorescence lifetime on the solvent polarity parameter could be beneficial for the accurate detection of micropolarity changes in biological systems. The polarity sensing ability of DC-Lyso was further probed in complex environments like doped polymer films (Fig. S7†).

TADF properties of DC-Lyso *in vitro*

To check the long-lived emission properties of DC-Lyso, we first recorded its emission under oxygenated and N_2-purged conditions (Fig. 2a). The transient photoluminescence measurements indicated the presence of microsecond time decay ($\tau_{avg} = 1.1$ μs) of the probe in deoxygenated DMSO solution at 298 K (Fig. 2a and S8a†). Moreover, the emission intensity ($\lambda_{em,max} \sim 640$ nm, DMSO) of DC-Lyso was enhanced upon prolonged N_2-purging (quantum yield, Q.Y. ~8%, Fig. 2a, inset) than under aerated conditions. The microsecond timescale decay was also observed in toluene ($\tau_{avg} = 2$ μs, Fig. S8b†). Time-resolved transient difference absorption spectra analysis of DC-Lyso in N_2-purged toluene solution upon 355 nm pulsed laser excitation revealed the presence of two distinct peaks at ~400 and 500 nm, referring to the ground state bleaching and excited state absorption, respectively (Fig. S9†). Similar excited state absorption peaks at the nanosecond and microsecond timescale suggest the involvement of the singlet excited state for the long-lived emission (Fig. S9†).[29]

Time-resolved emission spectra (TRES) measurements at 298 K also showed that the emission band originating at the nanosecond timescale (time delay: 5 ns) resembled the microsecond timescale (time delay: 1 μs) spectrum (Fig. 2b). Thus, the TRES measurements unambiguously ascertained a delayed fluorescence phenomenon in DC-Lyso either due to TADF or triplet–triplet annihilation (Fig. 2b, inset). The temperature-dependent emission spectra and decay analysis of DC-Lyso in toluene further demonstrated the thermal activation of the microsecond timescale emission (Fig. S10a–c).† The emission intensity gradually enhanced as the temperature was increased from 273 K to 333 K, a typical feature of TADF materials

(Fig. S10a†).[34,40] Moreover, the laser power-dependent emission study revealed unimolecular dependence of the delayed fluorescence emission (time delay = 1 μs),[36,37] confirming the TADF in DC-Lyso (Fig. S10d†).

The low-temperature measurements at 77 K further showed a red shift ($\lambda_{em,max}$ = 570 nm) as compared to the steady-state spectrum in toluene obtained at room temperature ($\lambda_{em,max}$ ~ 500 nm, Fig. 1b, S5a and S11a†). Photoluminescence decay analysis indicated the presence of a longer component at the millisecond time domain with an average lifetime (τ_{avg}) of 181 ms ($\lambda_{em,max}$ = 570 nm, Fig. S11b†), suggesting a phosphorescence emission. Further, time-resolved emission spectra (TRES) analysis at 298 K and 77 K was performed to reconstruct the onsets of fluorescence (time delay: 5 ns) and phosphorescence bands (time delay: 180 ms), respectively, which revealed a small ΔE_{ST} of 0.21 eV (Fig. S12 and Table S6†), corroborating well with the theoretically obtained data (Fig. S2a†).

To overcome the air-sensitive nature of the delayed fluorescence emission of DC-Lyso and to enhance its suitability for time-resolved imaging, the water-dispersible nanoaggregates (DCL-NPs) were prepared in 90% water–DMSO binary solvent mixture (Fig. 2c). DCL-NPs exhibited an absorption spectrum similar to that of DC-Lyso in the solution state (Fig. S13a†); the emission maximum of DCL-NPs centered at ~600 nm (Q.Y. ~ 10 ± 0.3%, Fig. 2c). The morphology of the nanoaggregates was visualized using transmission electron microscopy (TEM), revealing the distribution of spherical particles (diameter ~90 ± 20 nm, Fig. 2c, inset, Fig. S14†). The aqueous dispersion of the nanoaggregates showed an average prompt and delayed decay times of 15 ns and 20 μs, respectively (Fig. S13b and Table S7†). TRES measurements at the nanosecond and microsecond timescale suggested delayed fluorescence in DCL-NPs (Fig. 2c). Further, the delayed emission intensity (time delay = 1 μs) of DCL-NPs increased linearly with laser power (slope = 1.13, Fig. 2d, inset),[36,37] confirming it as TADF (Fig. 2d).

Cytotoxicity assay and cellular internalization

In order to evaluate the suitability of DC-Lyso for probing lysosomal polarity, the stability of the probe was verified under the lysosomal pH range (pH = 4.5–5.5, Fig. S18†). Furthermore, the exposure of DC-Lyso to different possible interfering agents like biologically relevant ions only resulted in negligible spectroscopic changes (Fig. S20†). MTT assay employing HeLa cells revealed no apparent cytotoxicity even after 24 h of incubation with DC-Lyso (1–40 μM, Fig. S21a†). Moreover, MTT assay suggested high cell viability (~80 ± 5%) at a working concentration of 2 μM after DC-Lyso incubation for 5 days (Fig. S21c†). The lower cytotoxicity was further verified using a more sensitive JC-1 assay based on the mitochondrial membrane potential,[22] demonstrating ~83% of healthy cells even after 24 h incubation with 10 μM DC-Lyso (Fig. S22†). Further, SYBR Green I-propidium iodide (PI) assay using HeLa cells under 405 nm laser irradiation (20 mW cm^{-2}) signified the low-phototoxicity effect of DC-Lyso (Fig. S23†). Thus, DC-Lyso is highly suitable for long-term lysosomal imaging due to its low cyto- and phototoxicity.

DC-Lyso exhibited fast cell-membrane permeability for live cells, as bright fluorescence signals were observed from HeLa cells incubated with the probe only for 1–10 min at 37 °C (Fig. 3a, S24 and S27†). The fast cell-membrane permeability of DC-Lyso encouraged us to investigate its cellular internalization mechanism (Fig. 3b–d). A small molecular probe like DC-Lyso could internalize within the cells following (i) passive diffusion across the cell membrane (dependent on the lipophilicity of the probe and driven by concentration and electric gradient), (ii) active transport (dependent on adenosine triphosphate consumption), or (iii) endocytic pathway (formation of specific compartments, energy-dependent and mostly inactivated at lower temperature). In the present case, significant fluorescence signals were observed from HeLa cells incubated at lower temperatures like 20 °C and 4 °C (Fig. 3c and S25†).[56] Further, similar fluorescence intensities in amiloride and chlorpromazine-treated cells, as compared to the control set of HeLa cells, ruled out the possibility of macropinocytosis and

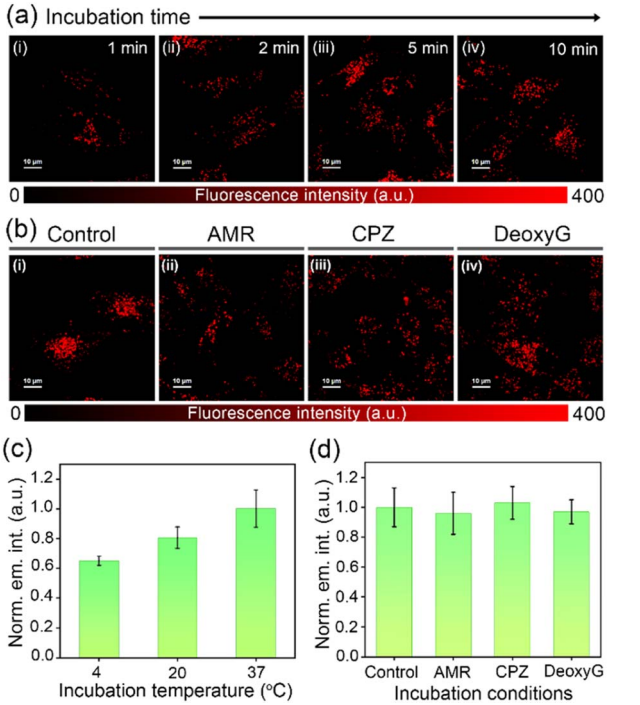

Fig. 3 (a) Time-dependent incubation studies of DC-Lyso (λ_{ex} = 405 nm, λ_{em} = 488–800 nm) stained HeLa cells depict the fast cell membrane permeability of the probe. (b) Confocal laser scanning microscopy (CLSM) images of DC-Lyso (10 min incubation, λ_{ex} = 405 nm, λ_{em} = 488–800 nm) in HeLa cells incubated with (i) complete growth media, considered as control, (ii) amiloride (AMR), (iii) chlorpromazine (CPZ), and (iv) deoxy D-glucose (DeoxyG) indicating similar intracellular fluorescence intensities. For (a, b) scale = 10 μm. Intracellular fluorescence intensity variation of DC-Lyso in HeLa cells incubated (c) at different temperatures, 4, 20, and 37 °C, and (d) in complete growth media (control), in the presence of macropinocytosis inhibitor amiloride (AMR), clathrin-mediated endocytosis inhibitor chlorpromazine (CPZ), and metabolic inhibitor deoxy D-glucose (DeoxyG) in fetal bovine serum (FBS)-free growth media at 37 °C and 5% CO_2 environment; error bars are plotted with respect to three independent measurements (n = 3).

clathrin-mediated endocytosis, respectively (Fig. 3b, d and S26†). Incubation of DC-Lyso in adenosine triphosphate (ATP) depleted cells (deoxy D-glucose incubation) revealed negligible intracellular fluorescence intensity variations as compared to the control cells, excluding the possibility of active transport (Fig. 3d and S26†).[56] Thus, passive diffusion is considered as the dominant cellular internalization mechanism for DC-Lyso.

Dynamic lysosomal polarity through lifetime imaging

The colocalization experiments were performed using HeLa cells stained with DC-Lyso along with the commercially available organelle tracker dyes (Fig. 4a, S27 and S28†). The intracellular fluorescence signals of DC-Lyso overlapped well with LysoTracker™ Green (LTG) for different incubation periods, suggesting the fast and specific lysosome targeting ability of DC-Lyso (Fig. 4a and S27†). The excellent lysosome selectivity of DC-Lyso was attributed to the weakly basic morpholine unit covalently linked to the TADF core.[2,10] DC-Lyso showed a higher intracellular photostability compared to commercial lysosome-specific probes like LTG and LysoTracker™ Red (LTR) under continuous laser irradiation of constant power (laser power = 10 μW, power density = 2 μW cm^{-2}, Fig. S31 and S32†) for 30 min. In addition to the high intracellular photostability, FLIM images of DC-Lyso revealed the diverse lifetime distribution in lysosomes, suggesting a promising scope for real-time tracking of lysosomal polarity (Fig. S34†).

To date, very few reports have demonstrated the long-term imaging of lysosomal dynamics and lysosome–organelle interactions.[7,9,57,58] DC-Lyso could retain in lysosomes for multiple days after single-time incubation (Fig. 4b and S35†). Such retention ability of DC-Lyso could be beneficial to monitor lysosomal function during physiological processes like cell division and migration. Pseudo-colored confocal laser scanning microscopy (CLSM) images at different time points, 4–24 min, ascertained the diverse spatial distribution of lysosomes within the cytoplasm (Fig. S36 and S37, Movie S1†). Lysosomal dynamics were also confirmed by merging the images obtained at different time points: 4 + 8, 8 + 12, 12 + 16, 16 + 24, and 4 to 24 min (Fig. S36†). FLIM images recorded during the lysosomal motions further displayed the subtle fluorescence lifetime variation of DC-Lyso (Fig. 4c, Movie S2†). The metabolite transfer during the lysosomal motions like fusion-fission and kiss-and-run presumably impart lysosomal microenvironmental changes leading to the subsequent polarity and lifetime variation.[1] The linear dependence of fluorescence lifetime on Reichardt's normalized solvent polarity parameter (E_T^N) thus provides new insights into lysosomal polarity fluctuations under physiological conditions (Fig. 4c and S6b†).

Real-time imaging of lysosomal polarity during autophagy

To decipher interorganelle interactions involving lysosomes, we monitored the lysosome-lipid droplet and lysosome–mitochondria interaction during autophagy.[14,59] The occurrence of lipophagy and mitophagy was confirmed by performing an autophagy assay in the presence of selective autophagy inducers like lipopolysaccharide (LPS) and carbonyl cyanide *m*-chlorophenyl hydrazone (CCCP), respectively (Fig. S38†).[59,60] HeLa cells costained with DC-Lyso and commercial lipid-droplet tracker dye BODIPY 493/503 were treated with LPS to induce lipophagy (Fig. 5). A significant enhancement in the Pearson's colocalization coefficient (PCC) values were observed in the LPS-treated cells (PCC: 0.62) than the control set of cells (PCC: 0.29, Fig. 5iv, ix, xiv, xix, S39–S41†). Moreover, PCC values increased from 0.43 (t = 10 min) to 0.62 (t = 60 min) in the LPS-treated cells (Fig. 5ix, xiv, xix). The FLIM images demonstrated that the average lifetime of DC-Lyso in the lysosomes first

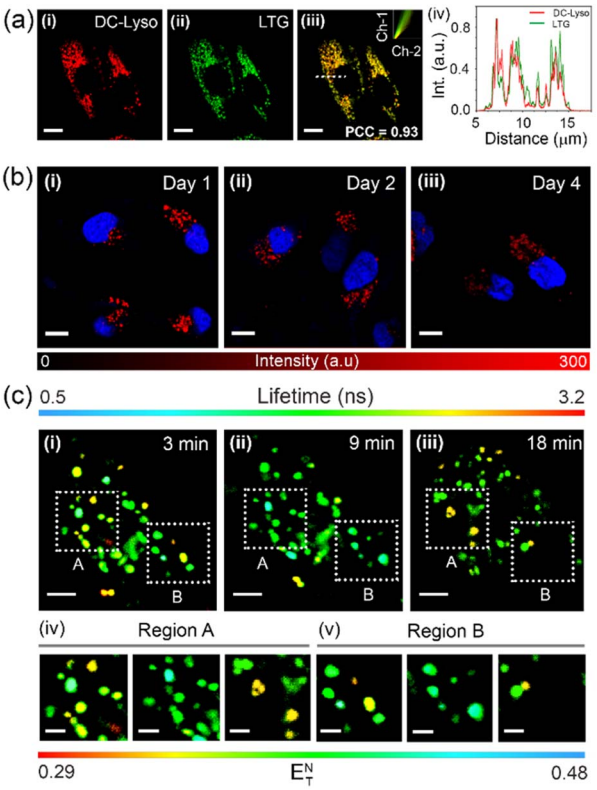

Fig. 4 (a) Colocalization study using confocal laser scanning microscopy (CLSM) of HeLa cells coincubated with (i) DC-Lyso (λ_{ex} = 405 nm, λ_{em} = 620–660 nm), (ii) LysoTracker™ Green (LTG, λ_{ex} = 470 nm, λ_{em} = 520–540 nm), and (iii) the merged image of (i) and (ii); inset: scatter plot of channel 1 (Ch-1) and channel 2 (Ch-2) depicts a high Pearson's coefficient of colocalization (PCC) value of 0.93, indicating lysosome targeting ability of the probe; scale = 10 μm. (iv) Intracellular intensity profiles of DC-Lyso and LTG for the dotted white line depicted in the image (iii) ascertaining colocalization of DC-Lyso with LTG in living cells. (b) Long-term imaging of HeLa cells employing DC-Lyso (λ_{ex} = 405 nm, λ_{em} = 620–660 nm) for single-time incubation; images of HeLa cells taken at (i) 1 day, (ii) 2 days, and (iii) 4 days after staining. The intracellular fluorescence intensity scale of DC-Lyso is also shown. Nucleus staining performed with 4′,6-diamidino-2-phenylindole (DAPI, λ_{ex} = 405 nm, λ_{em} = 400–445 nm) prior to imaging; scale = 10 μm. (c) Time-lapse fluorescence lifetime imaging microscopy (FLIM) images of HeLa cells stained with DC-Lyso (λ_{ex} = 405 nm and λ_{em} = 425–800 nm) highlighting the change in polarity during lysosomal dynamics at (i) 3, (ii) 9, and (iii) 18 min; scale = 4 μm; (iv, v) a clear variation of the lifetime and hence polarity during lysosomal dynamics represented by the normalized Reichardt's polarity parameter (E_T^N) of the corresponding zoomed portions (region A and B) of (i–iii); scale = 1 μm.

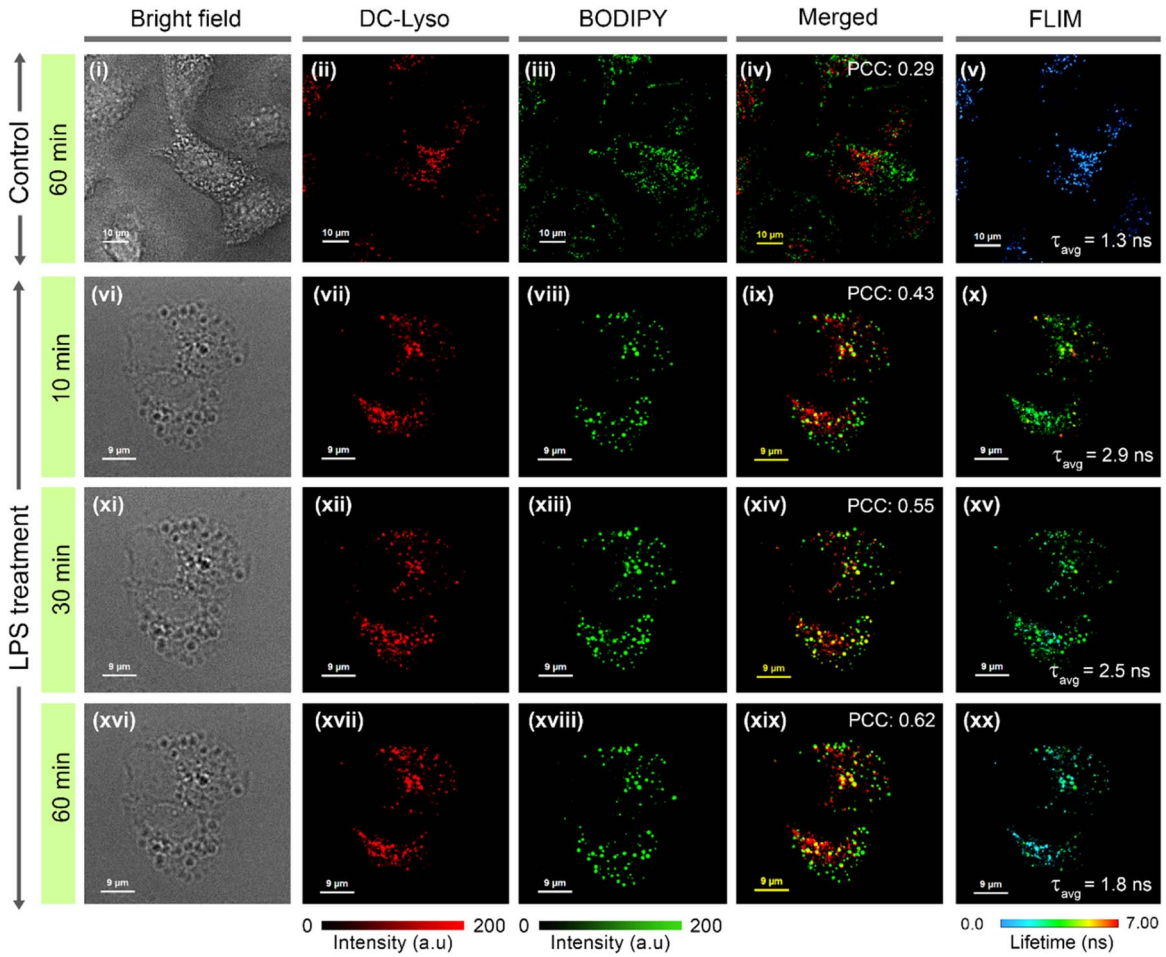

Fig. 5 Time-lapse confocal laser scanning microscopy (CLSM) imaging of lysosome-lipid droplet interactions in (i–v) control set ($t = 60$ min) and (vi–xx) lipopolysaccharide (LPS)-treated (to induce lipophagy) HeLa cells; (i, vi, xi, xvi) bright field images, cells incubated with (ii, vii, xii, xvii) DC-Lyso ($\lambda_{ex} = 405$ nm, $\lambda_{em} = 620–660$ nm), (iii, viii, xiii, xviii) commercial lipid droplet tracker dye, BODIPY 493/503 (BODIPY, $\lambda_{ex} = 470$ nm, $\lambda_{em} = 520–540$ nm), and (iv, ix, xiv, xix) corresponding merged images depict the gradual rise of Pearson's correlation coefficient (PCC = 0.43, $t = 10$ min; PCC = 0.55, $t = 30$ min; PCC = 0.62, $t = 60$ min after incubation with LPS) as compared to the control set of cells (without LPS treatment, PCC = 0.29, $t = 60$ min). (v, x, xv, xx) Corresponding FLIM images of DC-Lyso channel depicting the fluorescence lifetime variations in lysosomes during the lipid droplet–lysosome interaction (zoomed images shown in Fig. S40†); for (i–v) scale = 10 μm, (vi–xx) scale = 9 μm. A common intensity scale and lifetime scale, respectively, for CLSM and FLIM images are shown.

increased from 1.3 ns (control cells) to 2.9 ns ($t = 10$ min) and then decreased to 2.5 ns ($t = 30$ min) to 1.8 ns ($t = 60$ min) upon LPS treatment (Fig. 5v, x, xv, xx, and S40†). Consequently, an initial drop and the subsequent enhancement of the lysosomal polarity were observed (Fig. 5, S6 and S40†). The initial decrease in polarity, hence the increase in lifetime (Fig. 5v, x), was attributed to the interaction between hydrophobic (low polar) lipid droplets and high polar lysosomes.[6] The release of hydrolase enzymes, responsible for the degradation of the metabolites, was attributed to the recovery in the local polarity manifested by the decrease in the fluorescence lifetime from 30 to 60 min.[14,16] However, no visible changes in the fluorescence lifetime were observed in the cells without LPS treatment (Fig. S39†).

Further, we probed the lysosomal polarity variation during mitophagy, *i.e.*, lysosome-mediated mitochondrial disruption, one of the vital interorganelle interactions.[59,61,62] HeLa cells costained with DC-Lyso and commercial mitochondria tracker dye MitoTracker™ Green (MTG) were treated with a mitophagy inducer carbonyl cyanide *m*-chlorophenyl hydrazone (CCCP, Fig. 6a). Time-lapse images recorded at green and red channels indicated dynamics of mitochondria and lysosomes, respectively, in the control and CCCP-treated cells (Fig. 6a, S42 and S43†). Disruption to the long fibril-like structure of mitochondria was noticeable only upon CCCP treatment (Fig. 6a, i–iv and S43†). Moreover, the merged images of green and red channels showed a higher Pearson's coefficient for the CCCP-treated cells (PCC = 0.60, $t = 60$ min, Fig. 6a, vi and S43†) as compared to the CCCP-untreated cells (PCC = 0.41, $t = 60$ min, Fig. 6a, iii and S42†).

Time-lapse FLIM imaging revealed a longer lifetime component ($\tau_L \sim 4$ ns, $t = 10$ min) in the lifetime histogram of DC-Lyso after CCCP treatment, along with the shorter lifetime component ($\tau_S \sim 1.3$ ns, Fig. 6a and b) observed in normal

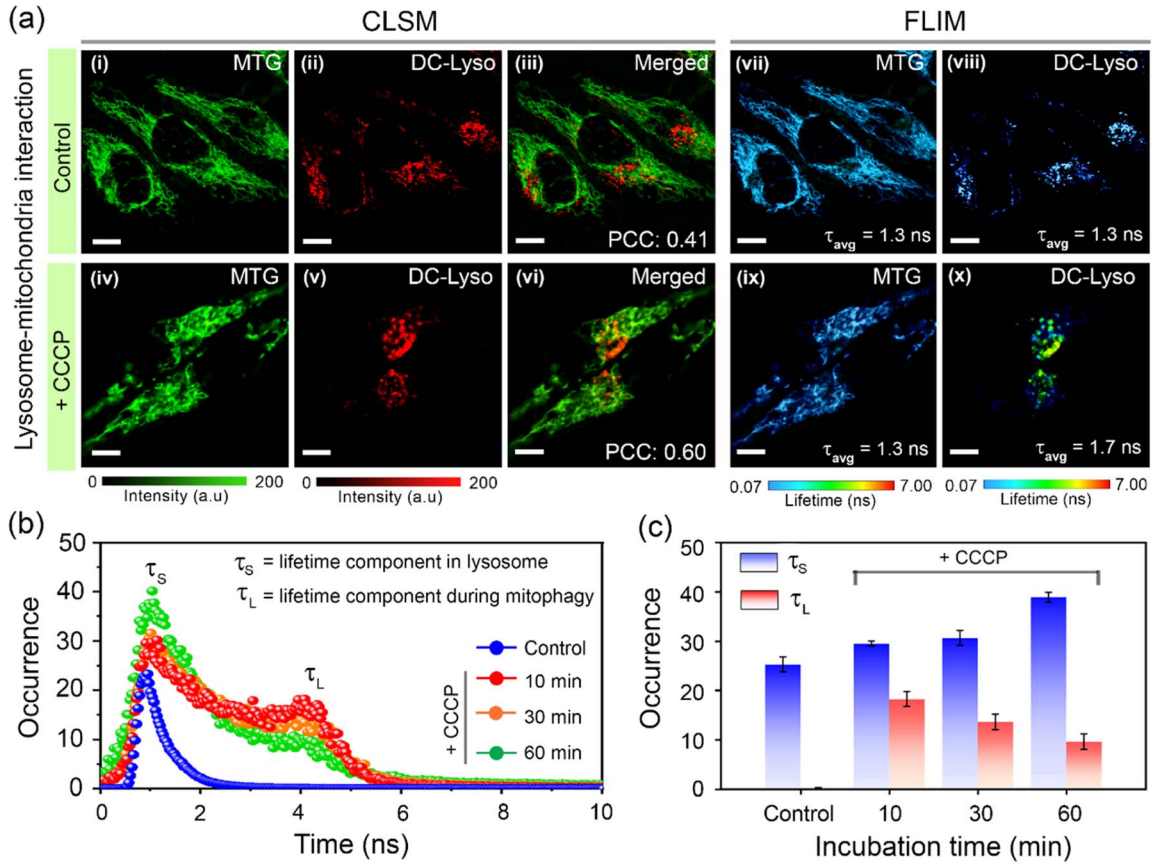

Fig. 6 (a) CLSM images of HeLa cells stained with (i, iv) commercial mitochondria tracker dye, MitoTracker™ Green (MTG, $\lambda_{ex} = 470$ nm, $\lambda_{em} =$ 520–540 nm), (ii, v) DC-Lyso ($\lambda_{ex} = 405$ nm, $\lambda_{em} = 620$–660 nm), and merged images of (iii) i and ii, and (vi) iv and v, indicating mitochondria–lysosome interaction (mitophagy) only after (iv–vi) carbonyl cyanide *m*-chlorophenyl hydrazone (CCCP) treatment. Corresponding FLIM images of HeLa cells stained with (vii, ix) MTG and (viii, x) DC-Lyso portray the variation of fluorescence lifetime after CCCP treatment only in the DC-Lyso channel; scale = 7 μm. The images (i–x) are recorded after 60 min from the incubation (5 min). (b) Representative lifetime histograms of HeLa cells stained with DC-Lyso without CCCP treatment (control) and with CCCP treatment (mitophagy) over gradual time intervals, suggesting the generation of a longer lifetime component ($\tau_L \sim 4$ ns) along with the shorter lifetime component ($\tau_S \sim 1.3$ ns). (c) Time-dependent variation of fluorescence lifetime in control and CCCP-treated HeLa cells stained with DC-Lyso. A relative decrease in the longer fluorescence lifetime component (τ_L, red) and an increase in the shorter fluorescence lifetime component (τ_S, blue) from the CCCP-treated HeLa cells indicate the increase in lysosomal polarity during mitophagy. The bar diagrams are plotted as mean ± standard deviation (three independent measurements).

lysosomes. This implied a relative decrease in lysosomal polarity during the initial interaction period with mitochondria. A close inspection of the lifetime histograms suggests an increase in the shorter decay component compared to the longer one over time ($t = 10$ to 60 min, Fig. 6b and c). Consequently, the initial decrease, followed by the recovery in the local polarity, was due to the release of hydrolytic enzymes upon lysosome–mitochondrion interaction.[14,16] The corresponding FLIM images of the control set of cells without CCCP treatment indicated no significant change in the fluorescence lifetime of DC-Lyso (Fig. S42 and S43†). The current results thus unambiguously demonstrate the time-resolved detection of subtle lysosomal polarity variation for the first time during lipophagy and mitophagy.

Lysosomal polarity as an indicator of aging

The potential of DC-Lyso to monitor subcellular polarity was further explored to decipher the aging process in the multicellular organism *C. elegans* (Fig. 7). It serves as a suitable model for elucidating the polarity-based changes in different organelles with aging due to the resemblance of age-related human orthologous gene sequences.[63,64] The gut granules of *C. elegans* have been classified as lysosome-related organelles (LRO) due to the presence of lysosomal proteins and staining with lysosome-specific fluorescent dyes like LysoTracker™.[65] CLSM imaging of *C. elegans* incubated with DC-Lyso for 2 h displayed distinct fluorescence signals from the worm body (Fig. 7b, S47 and S48†). Colocalization studies using DC-Lyso and LysoTracker™ Green confirmed the LRO targeting ability of DC-Lyso (Fig. S49†). We explored the inherent variations in lysosomal polarity with aging by staining wild-type *C. elegans* (N2 strain) at different developmental stages (L2, L3, and day-1 adult) of their lifespan (Fig. 7c, S50 and S51†). The FLIM images showed a sharp fluorescence lifetime distribution of ~3–5 ns of the probe in lysosome-related organelles of wild-type L2 stage worms (Fig. 7c, iii, and d). In contrast, the FLIM images of the

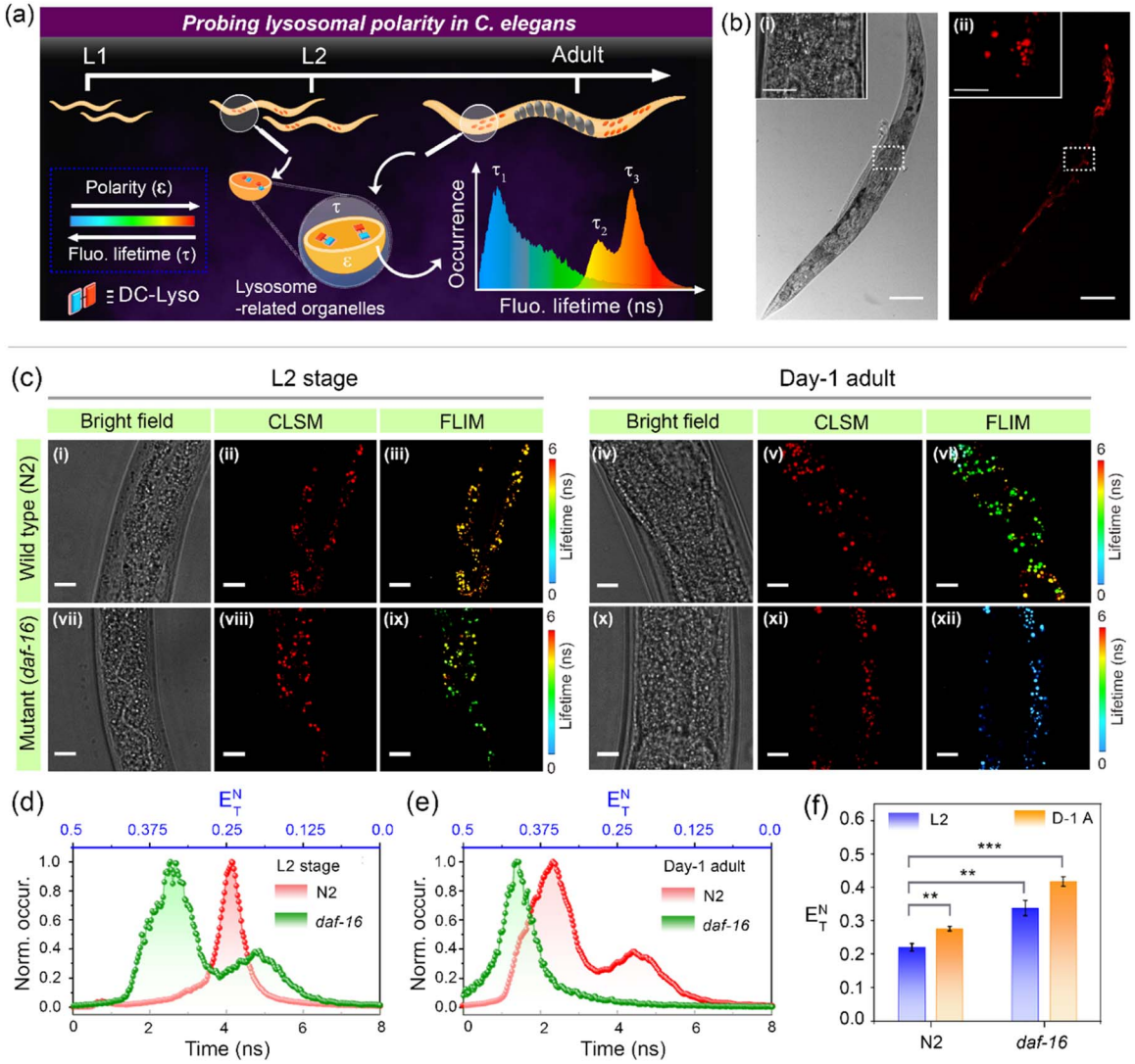

Fig. 7 (a) Schematic illustration depicting the polarity changes in lysosome-related organelles of *Caenorhabditis elegans* (*C. elegans*) at different developmental stages of their lifespan employing DC-Lyso. (b) CLSM imaging of DC-Lyso stained *C. elegans*: (i) bright field and (ii) red channel (λ_{ex} = 405 nm, λ_{em} = 570–660 nm) images; scale = 100 μm, inset: zoomed images of the selected portion shown in the white box; scale = 50 μm. (c) Intestinal lysosomal imaging of DC-Lyso stained (i–vi) wild-type (N2) and (vii–xii) short-lived mutant (*daf-16*, fast aging) strains. Images represent (i–iii, vii–ix) L2 and (iv–vi, x–xii) day-1 adult stages of the worms: (i, iv, vii, x) bright field, (ii, v, viii, xi) CLSM images, and (iii, vi, ix, xii) FLIM images (λ_{ex} = 405 nm, λ_{em} = 425–800 nm). The lower fluorescence lifetime of the probe indicates the high lysosomal polarity in adult worms in comparison to the L2 stage worms, and this difference is even more noticeable for the short-lived mutant (*daf-16*, fast aging). Fluorescence lifetime histograms of DC-Lyso revealed the lysosomal polarity changes represented by the normalized Reichardt's polarity parameter (E_T^N) in *C. elegans*: (d) L2 stage, and (e) day-1 adult; the histograms of wild-type (N2, red), and mutant (*daf-16*, green) worms are indicated. (f) Bar diagrams representing the lysosomal polarity variations in wild-type (N2) and fast-aging mutant (*daf-16*) *C. elegans* at different developmental stages of their lifespan [L2 and day-1 adult (D-1 A)]; the bar diagrams are plotted as mean ± standard deviation (n = 3) from the average lifetime values obtained from the decay plots for each data set. *P*-values are calculated by performing Student's *t*-test, where ** and *** denote $p < 0.01$ and $p < 0.001$, respectively.

day-1 adult worms revealed a broad lifetime distribution encompassing two distinct regions, one longer component (τ_L) at ~3–5 ns and another shorter component (τ_S) at ~1.5–3 ns (Fig. 7c, vi, and e). The lifetime histogram also suggests a relatively higher abundance of the shorter fluorescence lifetime component of DC-Lyso in adult worms, indicating enhanced polarity (Fig. 7e). These results ascertain the significant increase in the polarity of lysosome-related organelles during the age-based development in *C. elegans*.

Further, we confirmed the increase of lysosomal polarity with aging by performing studies on a short-lived (fast-aging) mutant strain, *daf-16*(*mu86*). The accelerated aging characteristics of *daf-16* mutants compared to the wild-type worms were also reflected by the FLIM images depicted in Fig. 7c (iii, ix, and vi, xii). The images of L2 stage mutant worms showed a similar lifetime distribution observed in the day-1 adult of the wild-type worms (Fig. 7c–e). Moreover, the fluorescence lifetime distribution in day-1 adult worms of *daf-16* mutant *C. elegans*

indicated a shorter lifetime component of ~1–2 ns (Fig. 7c, xii and e), signifying the enhanced polarity of lysosomes. The bar diagrams represent the relative lowering of fluorescence lifetime and subsequent enhancement of polarity at the different lifespans of wild-type and *daf-16* mutant worms (Fig. 7f). These results suggest the promising scope of the polarity-sensitive probe, DC-Lyso, for exploring the aging process (Fig. S52†).

In vivo delayed fluorescence imaging

The long-lived emission of DC-Lyso further prompted us to probe the lysosomal polarity at the microsecond timescale. We employed water-dispersible nanoparticles of DC-Lyso (DCL-NPs) for the time-resolved imaging of lysosomes in different cell lines (HeLa, A549, and CHO) and lysosome-related organelles in *C. elegans* (Fig. 2c, 8 and S53†). As depicted in Fig. 8a and b, bright red-fluorescence signals were observed from lysosomes after incubation of DCL-NPs in HeLa cells and *C. elegans*. The time-resolved images with a 1 μs time delay indicated no significant change in the luminescence intensity, suggesting the scope of DCL-NPs for autofluorescence-free bioimaging with a high signal-to-noise ratio (Fig. 8c and d). Moreover, the aqueous dispersion of nanoparticles could effectively circumvent the oxygen-mediated triplet quenching in living cells and organisms without the requirements of further post-synthetic modifications.[10,26] The FLIM images of DCL-NPs-stained cells and *C. elegans* revealed the heterogeneous lifetime distribution even at the microsecond time domain, indicating the diverse polarity of lysosomes (Fig. 8e and f). These findings further strengthen the applicability of TADF emitters for time-resolved intracellular sensing and imaging.

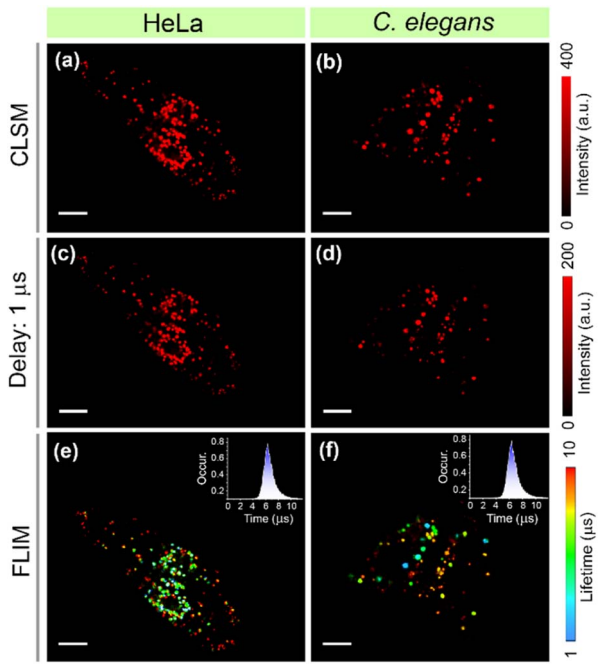

Fig. 8 Time-resolved imaging employing aqueous dispersion of DC-Lyso nanoparticles (DCL-NPs, $\lambda_{ex} = 470$ nm, $\lambda_{em} = 488–800$ nm) (a, c, e) HeLa cells, and (b, d, f) *C. elegans* (N2 strain). (a, b) CLSM images with no time delay, (c, d) time-gated images after applying a time delay of 1 μs, and (e, f) microsecond timescale FLIM images; scale = 10 μm; inset: the fluorescence lifetime histograms of DCL-NPs in lysosomes of (e) HeLa cells and (f) *C. elegans*.

Conclusion

In summary, a lysosome-specific thermally activated delayed fluorescent probe, DC-Lyso, was developed to monitor the subtle changes in cellular micropolarity under diverse physiological conditions. The large Stokes shift, rapid staining (1 min incubation), high photostability, and polarity-sensitive emission of DC-Lyso aided in background-free visualization of lysosomal dynamics through fluorescence lifetime imaging. To the best of our knowledge, the variation in lifetime distribution of DC-Lyso during lysosomal motions and lysosome-mediated autophagic pathways (lipophagy and mitophagy) revealed for the first time the intriguing polarity changes during lysosome–organelle interactions. Further, the lysosomal polarity changes during the developmental stages of a multicellular organism, *C. elegans*, suggests a higher polarity in the adult phase than in the younger worms. Thus, the present study opens up exciting avenues for thermally activated delayed fluorescent probes to unravel complex biological processes like aging with a high signal-to-noise ratio using intracellular time-resolved imaging.

Data availability

All experimental and characterization data are available in the ESI.†

Author contributions

S. D. developed the probe and performed all the spectroscopic experiments, FLIM imaging, tracking lysosomal dynamics, and interorganelle dynamics. A. B. helped in *C. elegans* experiments under the guidance of R. S. S. K., mentored S. D. in handling the microscope and provided fruitful suggestions. A. P. supervised and arranged the funding for the work. S. D. and A. P. wrote the manuscript, taking input from all the authors. All authors approved the final version of the manuscript.

Conflicts of interest

There are no conflicts to declare.

Acknowledgements

Infrastructural support from IISERB and financial support from BRNS, DAE (No. 37(2)/14/06/2016BRNS/37020) and the Council of Scientific and Industrial Research (CSIR), New Delhi (No. 01(2878)/17/EMR-II) are thankfully acknowledged. The live cell imaging system at the Department of Biology, IISERB and TEM facility at the Department of Chemistry, IISERB, supported through the DST FIST programme are also acknowledged. S. D. and A. B. acknowledge IISERB for the fellowship. S. D. acknowledges Ms. Nitu Saha and Ms. Dhanashri Rathod for their fruitful suggestions. The help during the laser fluence-

dependent study by Ms. Ashima Negi and Dr Ankur Gupta is gratefully acknowledged.

References

1 J. P. Luzio, P. R. Pryor and N. A. Bright, *Nat. Rev. Mol. Cell Biol.*, 2007, **8**, 622–632.
2 W. Xu, Z. Zeng, J. Jiang, Y. Chang and L. Yuan, *Angew. Chem., Int. Ed.*, 2016, **55**, 13658–13699.
3 J. Liu, W. Zhang, C. Zhou, M. Li, X. Wang, W. Zhang, Z. Liu, L. Wu, T. D. James, P. Li and B. Tang, *J. Am. Chem. Soc.*, 2022, **144**, 13586–13599.
4 J. Yin, L. Huang, L. Wu, J. Li, T. D. James and W. Lin, *Chem. Soc. Rev.*, 2021, **50**, 12098.
5 H. Zhu, J. Fan, J. Du and X. Peng, *Acc. Chem. Res.*, 2016, **49**, 2115–2126.
6 X. Zheng, W. Zhu, F. Ni, H. Ai, S. Gong, X. Zhou, J. L. Sessler and C. Yang, *Chem. Sci.*, 2019, **10**, 2342–2348.
7 F. Meng, J. Niu, H. Zhang, R. Yang, Q. Lu, Y. Yu, Z. Liu, G. Niu and X. Yu, *Sens. Actuators, B*, 2021, **329**, 129148.
8 X. Zhang, L. Yuan, J. Jiang, J. Hu, A. Rietz, H. Cao, R. Zhang, X. Tian, F. Zhang, Y. Ma, Z. Zhang, K. Uvdal and Z. Hu, *Anal. Chem.*, 2020, **92**, 3613.
9 Y. Han, M. Li, F. Qiu, M. Zhang and Y. Zhang, *Nat. Commun.*, 2017, **8**, 1307–1315.
10 S. Jaiswal, S. Das, S. Kundu, I. Rawal, P. Anand and A. Patra, *J. Mater. Chem. C*, 2022, **10**, 6141–6195.
11 H. Han, H. Tian, Y. Zang, A. C. Sedgwick, J. Li, J. L. Sessler, X. He and T. D. James, *Chem. Soc. Rev.*, 2021, **50**, 9391–9429.
12 L. Wang, Y. Xiao, W. Tian and L. Deng, *J. Am. Chem. Soc.*, 2013, **135**, 2903–2906.
13 M. Sardiello, M. Palmieri, A. di Ronza, A. D. L. Medina, M. Valenza, V. A. Gennarino, C. D. Malta, F. Donaudy, V. Embrione, R. S. Polishchuk, S. Banfi, G. Parenti, E. Cattaneo and A. Ballabio, *Science*, 2009, **325**, 473–477.
14 X. Li, X. Liang, J. Yin and W. Lin, *Chem. Soc. Rev.*, 2021, **50**, 102–119.
15 A. C. Sedgwick, L. Wu, H. Han, S. D. Bull, X. He, T. D. James, J. L. Sessler, B. Z. Tang, H. Tian and J. Yoon, *Chem. Soc. Rev.*, 2018, **47**, 8842–8880.
16 J. Zhang, X. Chai, X. He, H. Kim, J. Yoon and H. Tian, *Chem. Soc. Rev.*, 2019, **48**, 683–722.
17 F. M. Platt, A. d'Azzo, B. L. Davidson, E. F. Neufeld and C. J. Tifft, *Nat. Rev. Dis. Primers*, 2018, **4**, 27–51.
18 J. Zhou and H. Ma, *Chem. Sci.*, 2016, **7**, 6309–6315.
19 M. Y. Berezin and S. Achilefu, *Chem. Rev.*, 2010, **110**, 2641–2684.
20 K. Wang, L. Liu, D. Mao, S. Xu, C. Tan, Q. Cao, Z. Mao and B. Liu, *Angew. Chem., Int. Ed.*, 2021, **60**, 15095–15100.
21 N. Gupta, S. I. Reja, V. Bhalla, M. Gupta, G. Kaur and M. Kumar, *J. Mater. Chem. B*, 2016, **4**, 1968–1977.
22 S. Kundu, B. Sk, N. Saha, S. Das, T. K. Dutta, A. Batra, R. S. Tomar and A. Patra, *ACS Mater. Lett.*, 2023, **5**, 27–35.
23 A. S. Klymchenko, *Acc. Chem. Res.*, 2017, **50**, 366–375.
24 Z. He, H. Gao, S. Zhang, S. Zheng, Y. Wang, Z. Zhao, D. Ding, B. Yang, Y. Zhang and W. Z. Yuan, *Adv. Mater.*, 2019, **31**, 1807222.
25 X. Xiong, F. Song, J. Wang, Y. Zhang, Y. Xue, L. Sun, N. Jiang, P. Gao, L. Tian and X. Peng, *J. Am. Chem. Soc.*, 2014, **136**, 9590–9597.
26 F. Fang, L. Zhu, M. Li, Y. Song, M. Sun, D. Zhao and J. Zhang, *Adv. Sci.*, 2021, **8**, 2102970.
27 S. Qi, S. Kim, V. Nguyen, Y. Kim, G. Niu, G. Kim, S. Kim, S. Park and J. Yoon, *ACS Appl. Mater. Interfaces*, 2020, **12**, 51293–51301.
28 X. Li, G. Baryshnikov, L. Ding, X. Bao, X. Li, J. Lu, M. Liu, S. Shen, M. Luo, M. Zhang, H. Ågren, X. Wang and L. Zhu, *Angew. Chem., Int. Ed.*, 2020, **59**, 7548–7554.
29 D. Sasikumar, A. T. John, J. Sunny and M. Hariharan, *Chem. Soc. Rev.*, 2020, **49**, 6122–6140.
30 J. Chen, X. Chen, L. Cao, H. Deng, Z. Chi and B. Liu, *Angew. Chem., Int. Ed.*, 2022, **61**, e202200343.
31 B. Adelizzi, P. Chidchob, N. Tanaka, B. A. G. Lamers, S. C. J. Meskers, S. Ogi, A. R. A. Palmans, S. Yamaguchi and E. W. Meijer, *J. Am. Chem. Soc.*, 2020, **142**, 16681–16689.
32 S. Kuila, S. Garain, S. Bandi and S. J. George, *Adv. Funct. Mater.*, 2020, **30**, 2003693.
33 H. Shi, L. Zou, K. Huang, H. Wang, C. Sun, S. Wang, H. Ma, Y. He, J. Wang, H. Yu, W. Yao, Z. An, Q. Zhao and W. Huang, *ACS Appl. Mater. Interfaces*, 2019, **11**, 18103–18110.
34 H. Uoyama, K. Goushi, K. Shizu, H. Nomura and C. Adachi, *Nature*, 2012, **492**, 234–238.
35 Y. Im, M. Kim, Y. J. Cho, J. Seo, K. S. Yook and J. Y. Lee, *Chem. Mater.*, 2017, **29**, 1946–1963.
36 B. Sk, S. Sharma, A. James, S. Kundu and A. Patra, *J. Mater. Chem. C*, 2020, **8**, 12943–12950.
37 J. S. Ward, R. S. Nobuyasu, A. S. Batsanov, P. Data, A. P. Monkman, F. B. Dias and M. R. Bryce, *Chem. Commun.*, 2016, **52**, 2612–2615.
38 R. Hojo, D. M. Mayder and Z. M. Hudson, *J. Mater. Chem. C*, 2021, **9**, 14342–14650.
39 B. Kumari, R. Dahiwadkar and S. Kanvah, *Aggregate*, 2022, **3**, e191.
40 P. Data, P. Pander, M. Okazaki, Y. Takeda, S. Minakata and A. P. Monkman, *Angew. Chem., Int. Ed.*, 2016, **55**, 5739–5744.
41 S. Das, S. Kundu, B. Sk, M. Sarkar and A. Patra, *Org. Mater.*, 2021, **3**, 477–487.
42 Z. Zhu, D. Tian, P. Gao, K. Wang, Y. Li, X. Shu, J. Zhu and Q. Zhao, *J. Am. Chem. Soc.*, 2018, **140**, 17484–17491.
43 T. Li, D. Yang, L. Zhai, S. Wang, B. Zhao, N. Fu, L. Wang, Y. Tao and W. Huang, *Adv. Sci.*, 2017, **4**, 1600166.
44 F. Ni, Z. Zhu, X. Tong, W. Zeng, K. An, D. Wei, S. Gong, Q. Zhao, X. Zhou and C. Yang, *Adv. Sci.*, 2019, **6**, 1801729.
45 S. Sasaki, G. P. C. Drummen and G. Konishi, *J. Mater. Chem. C*, 2016, **4**, 2731–2743.
46 X. Liu, J. M. Cole and Z. Xu, *J. Phys. Chem. C*, 2017, **121**, 13274–13279.
47 C. Reichardt and T. Welton, *Solvents and Solvent Effects in Organic Chemistry*, Wiley-VCH Verlag GmbH & Co. KGaA, 2011.
48 S. I. Reja, I. A. Khan, V. Bhalla and M. Kumar, *Chem. Commun.*, 2016, **52**, 1182–1185.
49 Y. Zhang, Q. Ran, Q. Wang, Y. Liu, C. Hänisch, S. Reineke, J. Fan and L. Liao, *Adv. Mater.*, 2019, **31**, 1902368.

50 H. J. Park, C. W. Song, S. Sarkar, Y. W. Jun, Y. J. Reo, M. Dai and K. H. Ahn, *Chem. Commun.*, 2020, **56**, 7025–7028.
51 S. Kundu, A. Chowdhury, S. Nandi, K. Bhattacharyya and A. Patra, *Chem. Sci.*, 2021, **12**, 5874–5882.
52 K. Hayashi, A. Matsumoto and S. Hirata, *Chem. Commun.*, 2021, **57**, 1738–1741.
53 T. Wang, A. K. Gupta, S. Wu, A. M. Z. Slawin and E. Zysman-Colman, *J. Am. Chem. Soc.*, 2023, **145**, 1945–1954.
54 B. Sk, S. Khodia and A. Patra, *Chem. Commun.*, 2018, **54**, 1786–1789.
55 R. Hu, E. Lager, A. Aguilar-Aguilar, J. Liu, J. W. Y. Lam, H. H. Y. Sung, I. D. Williams, Y. Zhong, K. S. Wong, E. Peña-Cabrera and B. Z. Tang, *J. Phys. Chem. C*, 2009, **113**, 15845–15853.
56 K. Sugano, M. Kansy, P. Artursson, A. Avdeef, S. Bendels, L. Di, G. F. Ecker, B. Faller, H. Fischer, G. Gerebtzoff, H. Lennernaes and F. Senner, *Nat. Rev. Drug Discovery*, 2010, **9**, 597.
57 J. Hong, Q. Li, Q. Xia and G. Feng, *Anal. Chem.*, 2021, **93**, 16956–16964.
58 X. Chao, Y. Qi and Y. Zhang, *ACS Sens.*, 2021, **6**, 786–796.
59 S. Kundu, S. Das, S. Jaiswal and A. Patra, *ACS Appl. Bio Mater.*, 2022, **5**, 3623–3648.
60 A. Rogalska, A. Gajek, M. Łukawska, I. Oszczapowicz and A. Marczak, *PloS One*, 2018, **13**, e0201296.
61 F. Hu, X. Cai, P. N. Manghnani, Kenry, W. Wu and B. Liu, *Chem. Sci.*, 2018, **9**, 2756–2761.
62 S. Zeng, W. Shao, Z. Yu, L. Fang, G. Tang, Y. Fang, S. Chen, Z. Huang, J. Tan and X. Chen, *ACS Sens.*, 2023, **8**, 40–50.
63 H. A. Tissenbaum, *J. Gerontol., Ser. A*, 2012, **67**, 503–510.
64 Y. Sun, M. Li, D. Zhao, X. Li, C. Yang and X. Wang, *eLife*, 2020, **9**, e55745.
65 G. J. Hermann, L. K. Schroeder, C. A. Hieb, A. M. Kershner, B. M. Rabbitts, P. Fonarev, B. D. Grant and J. R. Priess, *Mol. Biol. Cell*, 2005, **16**, 3273–3288.